Experimental systems implementation of a hybrid optical–digital correlator

James H. Sharp, Nick E. MacKay, Pei C. Tang, Ian A. Watson, Brian F. Scott, David M. Budgett, Chris R. Chatwin, Rupert C. D. Young, Sylvie Tonda, Jean-Pierre Huignard, Tim G. Slack, Neil Collings, Ali-Reza Pourzand, Marcus Duelli, Aldo Grattarola, and Carlo Braccini

A high-speed hybrid optical–digital correlator system was designed, constructed, modeled, and demonstrated experimentally. This correlator is capable of operation at approximately 3000 correlations/s. The input scene is digitized at a resolution of 512 × 512 pixels and the phase information of the two-dimensional fast Fourier transform calculated and displayed in the correlator filter plane at normal video frame rates. High-fidelity reference template images are stored in a phase-conjugating optical memory placed at the nominal input plane of the correlator and reconstructed with a high-speed acousto-optic scanner; this allows for cross correlation of the entire reference data set with the input scene within one frame period. A high-speed CCD camera is used to capture the correlation-plane image, and rapid correlation-plane processing is achieved with a parallel processing architecture. © 1999 Optical Society of America

OCIS codes: 070.4550, 070.5040.

1. Introduction

Optical correlation promises high-speed object recognition and identification for applications as diverse as target acquisition, fingerprint verification, and process and quality control. Many of the obstacles that have, in the main, retarded the transition of optical information processing from laboratory-based work to real-world applications and environments have been technology based. Developments in spatial light modulator (SLM) technology in particular have greatly improved operating speeds and the overall feasibility of correlator application.[1–3] Over the years efforts have also been made to improve discrimination performance while retaining robustness to distortions in the input image. This has mainly been in the form of the development of filters for application in the correlator Fourier plane with particular emphasis being directed toward filter multiplexing and bandpassing for optimization of filter response.[4–10] These techniques often produce filters with the requirement for fully complex modulation in the correlator filter plane, not possible with currently available SLM technology.

The approach proposed by Young *et al.*[11] of using a hybrid optical–digital correlator system was adopted to avoid the requirement for a high-frame-rate phase-modulating frequency plane SLM. Given that the input scene of most real-time applications arrives at video frame rates, Young *et al.* proposed the use of a digital system to calculate the phase component of the Fourier transform (FT) of the input scene with

When this research was performed, J. H. Sharp (j.sharp@mech.gla.ac.uk), N. E. MacKay, P. C. Tang, I. A. Watson, and B. F. Scott were with the Laser and Optical Systems Engineering Centre, Department of Mechanical Engineering, James Watt Building, University of Glasgow G12 8QQ, UK. D. M. Budgett, C. R. Chatwin, and R. C. D. Young were with the School of Engineering, University of Sussex, Falmer, Brighton BN1 9Q2, UK. S. Tonda and J.-P. Huignard were with the Laboratoire Central de Recherches, Thomson-CSF, Domaine de Corbeville, 91404 CEDEX, France. T. G. Slack was with the Department of Optics and Laser Technology, Sowerby Research Centre, British Aerospace (Operations) Ltd., FPC 267, P.O. Box 5, Filton, Bristol BS12 7QW, UK. N. Collings, A.-R. Pourzand, and M. Duelli were with the Institute of Microtechnology, University of Neuchâtel, Rue A-L Breguet 2, CH-2000, Neuchâtel, Switzerland. A. Grattarola and C. Braccini were with the Department of Communication, Computer and Systems Sciences, Università degli Studi di Genova, Via Opera Pia 13, 16145 Genoa, Italy. P. C. Tang is now with the Department of Control Engineering, National Chiao-Tung University, Hsin-Chu, Taiwan. Marcus Duelli is now with the Electro-Optics Research Institute, Academic Building, University of Louisville, Louisville, Kentucky 40292.

Received 4 January 1999; revised manuscript received 28 June 1999.

0003-6935/99/296116-13$15.00/0

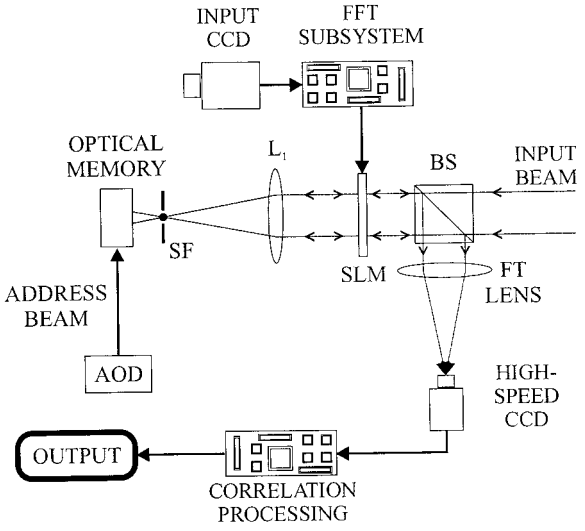

Fig. 1. Schematic representation of the compact phase-conjugating correlator system. BS, beam splitter; L, lens; SF, spatial filter.

direct display on a twisted nematic liquid-crystal (video-rate) phase-modulating SLM in the correlator filter plane. Reference templates are stored optically in a volume holographic angle-multiplexed holographic memory[12,13] and can be addressed at extremely high rates, producing as many as 3000 correlations/s. The technology to process and extract meaningful information from the correlation plane at these rates has been demonstrated.[14]

The optical system in the original proposal was that of a transposed 4*f* VanderLugt-style correlator. This brings with it concomitant implementation difficulties that are principally due to the requirement to match the phase spectra of the optically derived FT and the digitally calculated fast FT (FFT) to produce the desired correlation output. This may not be a trivial issue, since most of the widely used SLM's, such as those derived from the Seiko-Epson liquid-crystal television projector, have a nonunity aspect ratio. Other aspects of device performance, such as phase distortion due to SLM nonflatness, nonlinear phase response, residual amplitude coupling, and so on, also have implications for the ultimate performance one can obtain from the system. We have, therefore, used the compact phase-conjugating correlator devised by Duelli *et al.*[15] to overcome most of these problems in conjunction with the hybrid concept to produce a high-speed correlator system.

2. Overall System Description

A schematic of the compact phase-conjugating correlator system is shown in Fig. 1. Unlike conventional correlator geometries such as the VanderLugt, the input scene is captured by a CCD camera at a resolution of 512 × 512 pixels and its FT calculated digitally with a custom-built FFT processor board. This calculates the FFT of the image and then the phase spectrum that is applied to the correlator filter plane SLM. This phase image is updated at 25 frames/s, synchronized with the Comité Consultif International Radio (CCIR) camera observing the input scene. Since no rapid-frame-rate SLM's are currently available that offer a full 2π phase modulation, using the digitally calculated phase spectrum of the input scene at the filter plane rather than at the input plane facilitates the most effective use of the relatively slow SLM device.

The phase spectra of the reference templates are calculated numerically at a resolution of 512 × 512 pixels and stored as angle-multiplexed volume holograms in the optical memory with the aforementioned SLM as a phase-only display device. Since the SLM resolution is limited to 320 × 264 pixels, a common interpolation scheme is used in scaling the display during both image recording and correlator operation. Images are addressed with an acousto-optic deflector (AOD) and effectively placed at the correlator input plane. It is the rapid access of the template database in the optical memory offered by the AOD that provides the capability of high-speed correlator operation. Spatial filtering of the images is employed prior to storage in the optical memory to remove the dc bias of the image spectrum with a point stop filter. Note that the holograms stored are neither pure-space nor frequency-domain images; as shown in Fig. 5 below, a diverging beam is used, and, owing to the phase-conjugating nature of the design, during reconstruction any imperfections in this part of the optical train can readily be compensated.

The memory addressing beam reconstructs the phase conjugate of the stored hologram at the filter-plane SLM where the phase-only correlation with the current SLM image is obtained in the correlation plane. This is accomplished with a simple FT lens (L3 in Fig. 5) producing the correlation plane at the high-speed CCD camera. The correlation-plane capture and processing is performed with a high-speed, frame-transfer digital camera coupled to a custom-built imaging board that employs a parallel pixel processing architecture.[14] Output from this system provides information on correlation-peak position and an assessment of correlation-peak quality. Both the FFT subsystem and the correlation plane processing hardware are integrated in a single control system hosted in a personal computer (PC).

3. Optical Subsystems

A. Volume Holographic Memory

1. Image Handling

Given that angular orientation of the target object is unconstrained in the input scene, it is necessary to compile a reference data set representative of the unconstrained object. To this end, images of the test object are acquired for a full 360° in plane rotation in 5° increments and a 90° out-of-plane rotation in 10° increments. The test component (in the current study, a camshaft bearing cap) is placed at the end of the robotic actuator and located in an enclosure that provides uniform illumination conditions. The cam-

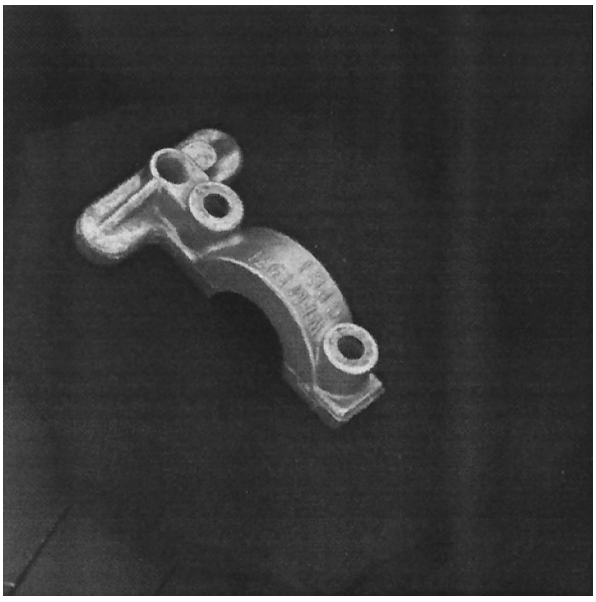

Fig. 2. Sample image of the test component for storage in the optical memory.

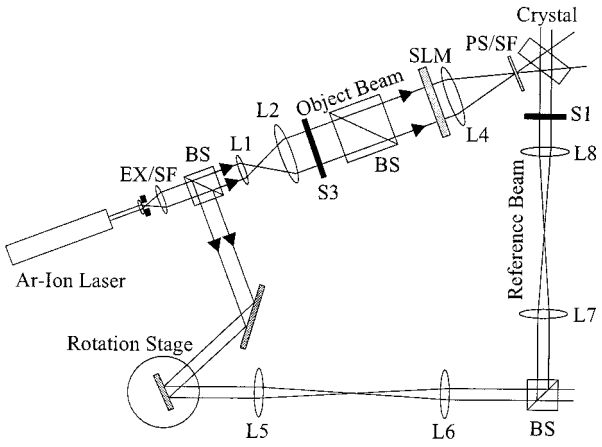

Fig. 3. Optical memory recording configuration. BS, beam splitter; EX, expander; L, lens; PS, point stop; S, shutter; SF, spatial filter.

era, placed at the top of this enclosure, is fitted with a motorized zoom lens for repeatable control of the object scaling. Overall control and synchronization of the image-acquisition process is achieved by use of a PC with custom software and frame-grabbing hardware. The process of obtaining each full data set of 512×512 pixel images is fully automated for convenience. The control software also generates an index file at the end of the capture process that contains positional and reference details of each image for import into a propriety database engine facilitating image selection and compilation as input into the optical memory recording system. Figure 2 shows a sample of a captured image of the test component.

Reference images are also used in the construction of correlation filters to be stored in the optical memory.[16] In this study optimal trade-off synthetic discriminant function filters (OT-SDF's) were constructed to reduce the correlator sensitivity to object rotation and input scene background. These complex filters were then computationally modified to the specific characteristics of a chosen SLM (whose coding domain contains only real values) for implementation in the correlator and these suboptimal filters recorded in the optical memory.

2. *Optical Memory Recording*

Fe:$LiNbO_3$ was selected as the most appropriate storage medium for this particular optical memory application, since it provides reasonably long storage times after fixing and is readily available and easy to work with. Crystals were sourced from three suppliers for comparison of performance and quality.[17] Doping concentrations and dimensions varied. However, typically, 10 mm $\times$ 10 mm $\times$ 7 mm crystals were used with 0.1-wt.% iron doping. Both y-cut and 45°-cut crystal were examined, with the y-cut geometry being employed in the system implemented.

Figure 3 shows the experimental configuration used for the recording system of the optical memory. The actual recording procedure is automated, owing to the relatively long total exposure times with large image sets. A Spectra-Physics Beamlok Model 2050 argon-ion laser is used for recording the holograms with a $\lambda/2$ wave plate used to rotate the plane of polarization of the laser output to optimize photorefractive response from the Fe:$LiNbO_3$ crystal. The beam is expanded and spatially filtered to provide a clean Gaussian beam that matches the crystal dimensions. The angular position of the reference beam is controlled with a mirror mounted on an Aerotech Model ADR150 rotation table providing an angular resolution of 3.6 μs of arc. A standard $4f$ optical system is used to transfer this beam to the crystal during recording. The AOD is not used during recording, because of the small, variable Doppler frequency shift introduced during deflection. This gives rise to an optical heterodyne if combined with the reference beam and hence a nonstationary interference pattern during hologram recording.

The object beam is further expanded to match the dimensions of the SLM and is then spatially filtered to remove the zero and higher orders that result from pixelation from the object image. The resulting edge-enhanced image is recorded in the optical memory as a volume phase hologram (see Fig. 4). Note that, for the purposes of evaluating the fidelity of the optical memory and reconstruction optics, space-domain images are used, whereas for correlator operation, phase images from the frequency domain are recorded. Figure 4(d) shows the projection of the phase-conjugate image at the SLM plane. Automation is again achieved by means of computer control with the shutter, rotation table, and SLM all being directly addressed by the PC. Custom hardware controlled by means of the PC industry-standard architecture (ISA) bus is used to provide output to the

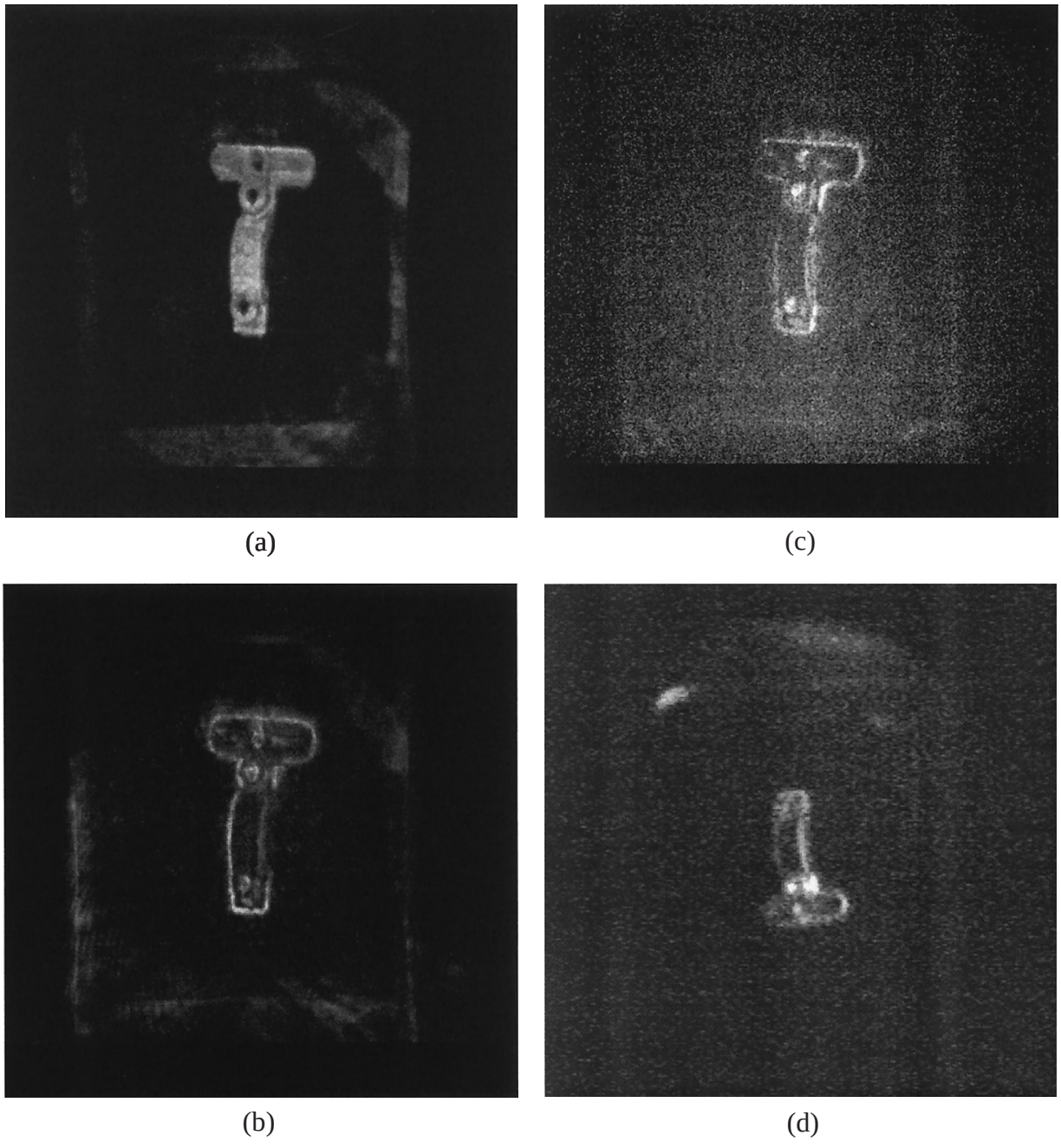

Fig. 4. Images from the optical memory. (a) Original image, (b) edge-enhanced original after spatial filtering, (c) reconstruction of edge-enhanced image, (d) phase-conjugate reconstruction.

SLM and, if required, can control pixel aspect ratio and also correct for phase nonuniformity in both static and dynamic response modes, all in real time.

During recording exposure, scheduling is necessary, since the recording of any given memory page partially overwrites any previous pages already present in the memory. Both the scheduled recording scheme with the algorithm of Mok *et al.*[18] and incremental recording[19] are available as system options. The photorefractive response of available crystals has been characterized[20] and a comparison between these schemes made. It was found that both techniques provided similar results, each with its own advantages and disadvantages. The sensitivity of the scheduling exposure algorithm to errors in measurements of the material response times is offset by the need for only one recording iteration. The iterative recording approach of the sequential method imposes stringent repeatability requirements on the angular positioning of the reference beam. Accurate return to the Bragg-matching position of each hologram for each iteration is required in order to reinforce rather than overwrite that particular hologram. However, it has been reported that the gray-scale fidelity with the incremental technique is significantly better,[20] and, owing to the accuracy

and the repeatability available from the system hardware, this is the recording scheme that is recommended.

3. Optical Memory Addressing

The reference images for the optical correlator are stored as angularly multiplexed holograms within the optical memory, and as such, issues regarding light utilization during reconstruction had to be considered prior to construction of the memory addressing system. Modeling of the holographic memory was undertaken with analysis based on the coupled-wave theory as derived for lossless, thick, phase gratings by Kogelnik.[21]

The maximum diffraction efficiency obtainable when Bragg matched to the grating is given by

$$\eta_{\max} = \sin^2\left(\frac{\pi \Delta n d}{\lambda \cos B}\right), \tag{1}$$

where d is the crystal thickness, λ the laser wavelength, B the angle of incidence that satisfies the Bragg condition, and Δn the photorefractive induced change in refractive index. Considering the angular response of any given hologram as one moves away from Bragg matching allows one to calculate the necessary accuracy for the addressing system and the implications for the total amount of energy available to form the correlation-plane image. The angular tolerance was chosen to be the deviation giving 90% or more of the peak diffraction efficiency for any given hologram. Numerical modeling of this indicates that this tolerance is approximately one fifth of the full peak width of the sinc^2 function that describes the diffraction efficiency falloff with angle. When one uses the mechanical system, and a step-and-hold method with the AOD, in an ideal addressing system it would be possible to ensure that each resolvable readout angle matched the center of the hologram's response. This would involve the optimization of the angular spacing between holograms, the correct alignment of the AOD, and no subsequent drift in the AOD's operation. If the perfect alignment and stable operation of the AOD cannot be relied on, then, to guarantee at least 90% diffraction efficiency from every hologram, the holograms' angular peaks must have a width of at least 5 times the AOD's angular resolution. The number of holograms capable of being addressed with the AOD in the system described here is the limiting factor in determining the useful storage capacity of the memory, which is only 750. However, the angular resolution is approximately 11 arc sec, and repeatability and accuracy are well within the predicted tolerances for the configurations used in the system. Long-term drift performance of the device is not specified and is currently under study.

One can usefully compare the performance of the adopted AOD addressing scheme with that of a raster scan approach, using a mechanical system such as a rotating polygon mirror. The above alignment issue does not apply if the read beam is scanned in a continuous fashion across the angular range containing the hologram's response. For a steady scanning rate the increasing beam angle can be replaced with an increase in time. The amount of time that it takes the beam to cross each peak will be dictated by the frame rate of the detector in the correlation plane and by the number of holograms to be integrated in each frame. For the current system it is intended that each hologram be interrogated for only a fraction of the detector frame time, with several correlation peaks being summed together. Angular separation between holograms is a trade-off between multiplexing density and cross talk; it is assumed that the separation will be the peak of one sinc^2 function coincident with the first zero of the next.

If, with the step-and-hold method described above, the read beam were aligned with a hologram response for t s, the energy available to the correlator would be

$$E_1 = P \eta_{\max} t, \tag{2}$$

where P is the laser power in watts incident on the hologram.

However, if the beam were scanned across the peak in the same time, the energy available would be

$$E_2 = P \int_0^t \eta(t)\mathrm{d}t = P \int_0^t \frac{\sin^2[\nu^2 + \xi(t)^2]^{1/2}}{1 + \xi(t)^2/\nu^2}\,\mathrm{d}t, \tag{3}$$

where

$$\xi(t) = \frac{(\gamma t - B)\pi \mathrm{d}}{\Lambda}, \qquad \nu = \frac{\pi \Delta n d}{\lambda (c_R c_S)^{1/2}},$$

$$c_R = \cos\theta, \qquad c_S = \cos\theta - \frac{\lambda \cos\phi}{\Lambda n},$$

and n is the refractive index of the crystal, Λ the period of the Bragg grating, θ the external angle of incidence of the read beam to the crystal, ϕ the angle between the crystal z axis and the grating normal, and γ the scan rate in radians/second.

To evaluate the integral shown in Eq. (3), the angular selectivity curve between the first two 0 points of the appropriate sinc^2 function in Eq. (1) is divided into 1024 samples. It is assumed that the time between these two points represents t s. The diffraction efficiency function is evaluated at each of the sample points and the results summed. The area under the curve is thus computed to be $0.16 \times t$. This then, when multiplied by the power in the laser beam, would represent the total energy available to the correlator as the beam is scanned across the hologram's angular selectivity profile. In comparison, the energy available if the read beam were held at the Bragg angle for a time of t s would be the product of the maximum diffraction efficiency, the laser power, and t; i.e., $0.37 \times t$. So scanning across the hologram profile, as opposed to holding the beam at the Bragg angle, reduces the correlation-plane energy by 66%. This is independent of the actual grating parameters

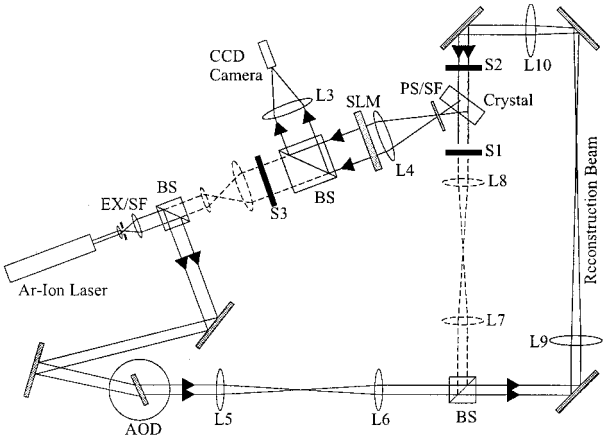

Fig. 5. Experimental configuration used when addressing the optical memory to reconstruct the phase conjugate of the stored image. BS, beam splitter; EX, expander; L, lens; PS, point stop; S, shutter; SF, spatial filter.

and the actual value of t but is true only if this latter quantity is less than the correlation-plane detector's frame time. It is apparent, then, that an approach of scanning the read beam across a peak incurs a penalty in the form of reduced energy in the correlation plane. However, the correlation signal produced by each hologram is always repeatable.

The experimental arrangement used during image reconstruction is shown in Fig. 5. This scheme provides angular displacement of the reconstruction beam equal to that used during recording for the reference beam while producing a phase-conjugate image. During reconstruction the mirror on the rotation stage is replaced with a high-speed Isomet Model LS-110 AOD, which provides a random access time of approximately 15 μs for each memory page. The clear aperture of this device has a 9.3-mm diameter with a scan angle of 2.4°, and the time–bandwidth product is specified as 750. Diffraction efficiency is greater than 60% across this scan range. After recording of the memory data, the combined diffraction efficiency of the AOD and the memory pages is characterized and a lookup table generated to flatten the overall diffraction response from the memory subsystem. This ensures uniformity in page reconstruction strength.

As well as the reference image each page of the optical memory also carries an encoded signal to provide an indication of the image address space. Since the input images are square, there is available SLM real estate at the edges of each page image, which is used to include an 8-bit binary encoding scheme, which may be easily extended to 12 or 16 bit as required. Since the recording system and the reconstruction system are different, an initial calibration procedure to find the angular positions of the memory pages is performed. This autocalibration generates an address lookup table that stores the appropriate voltages for each angular position of the reference image data set.

B. Phase-Modulating Spatial Light Modulator

The SLM's used in the correlator were extracted from a Seiko-Epson liquid-crystal video projector, Model VP-100PS. This device has an active area of 320 $\times$ 264 pixels, 25.5 mm $\times$ 19.1 mm in size. Each pixel is 55.9 μm $\times$ 51.5 μm with a pitch of 79.8 μm horizontally and 75.4 μm vertically. Previous researchers have demonstrated that more than 2π rad of phase modulation is available from these devices.[22] To extract the best performance from the SLM's, both during the recording of the reference images and during correlation, the optical responses of these devices were characterized and the device driver optimized to operate in the phase-modulating regime with maximum dynamic range. Although characteristics of these devices have been published previously,[23–26] from experience it was found that optimization required the individual assessment of each device.

Phase-modulation characteristics of the SLM's were measured with a wave-front-splitting interferometer.[27] The SLM is covered with an intensity mask of two small holes and illuminated with a plane wave. A Fourier lens is used to focus the output beams from the holes to form an interference pattern that is magnified by a microscope objective onto a CCD camera. The drive voltage applied to the area of the SLM behind the first hole is held constant while the drive voltage of the area behind the second hole is increased by stepping up of the gray-level value of a filled rectangle displayed on this area of the SLM. The phase lag introduced by the SLM versus the applied drive voltage can be extracted from the displacement of the measured interference pattern. Any coupled amplitude modulation can be extracted from the same pattern or be measured with a detector placed directly in the optical path of the changing beam.

Within each video projector, three SLM's are available, one for each of the color channels: red, green, and blue. These devices were initially characterized in terms of flatness and phase response. Measurements indicate that the best performance is consistently obtained from the green channel SLM, and consequently green SLM's were chosen as the best choice as the filter plane SLM for construction of the correlator. Typical results are shown in Appendix A for the red, green, and blue channel SLM's, respectively.

To achieve the desired modulation regime (for example, a phase lag of at least 2π with a constant transmittance), the dynamic range of the applied drive voltage must be large enough. The original SLM driver supplies a restricted voltage range designed for amplitude modulation. A custom-made driver was built to achieve the desired dynamic range. This driver enables one to tune the offset voltage and the amplitude of the incoming video signal, which is subsequently applied to the pixels of the SLM.

Figure 6 shows the phase modulation and the transmittance of a SLM derived from a blue channel

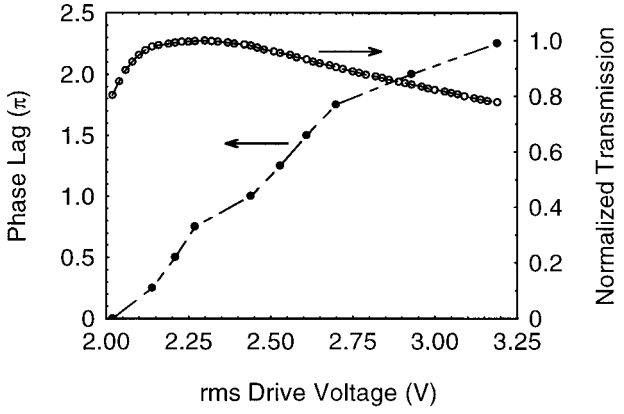

Fig. 6. Phase lag and transmittance of a blue channel SLM versus applied rms voltage.

SLM versus the rms applied drive voltage. This voltage is the rms value of the video signal at the output of the driver when the entire SLM is set to a single gray-level value (0–255). It is apparent from this figure that, for a phase lag in the region of $0–2\pi$, the residual amplitude modulation is relatively small. This characteristic is, of course, device dependent and is required for each device intended for use in the correlator.

When the available processing time for digital FFT calculation is increased, optical memory search strategies and correlation-plane processing are possible, should they be required. This is achieved by means of displaying the image on the SLM at twice the normal rate and holding for the remainder of the normal frame period. A second SLM driver was therefore modified to enable the SLM to be updated at a higher frame rate. With a CCIR 50-Hz video standard, it takes 20 ms for the calculated phase image from the FFT board to be displayed on the SLM. Given that the next video field also takes 20 ms and overwrites the first field, and assuming that the second video field is identical to the first, this time can be used for any additional processing tasks. Running the SLM with a 100-Hz video signal decreases the first video field display time to 10 ms. Because of the AABB algorithm[28] used for converting the 50-Hz signal to a 100-Hz signal, the three following fields are identical to the first. Hence the available processing time will be increased from 20 to 30 ms, and the duty cycle of the system is increased from 50% (with a 50-Hz signal) to 75% (with a 100-Hz signal). The driver has the facility to handle either 50- or 100-Hz video standards. Experimental results from assessing the optical response of the SLM's when driven at this rate (as shown in Fig. 7) indicate that the SLM's will operate satisfactorily at this frequency.

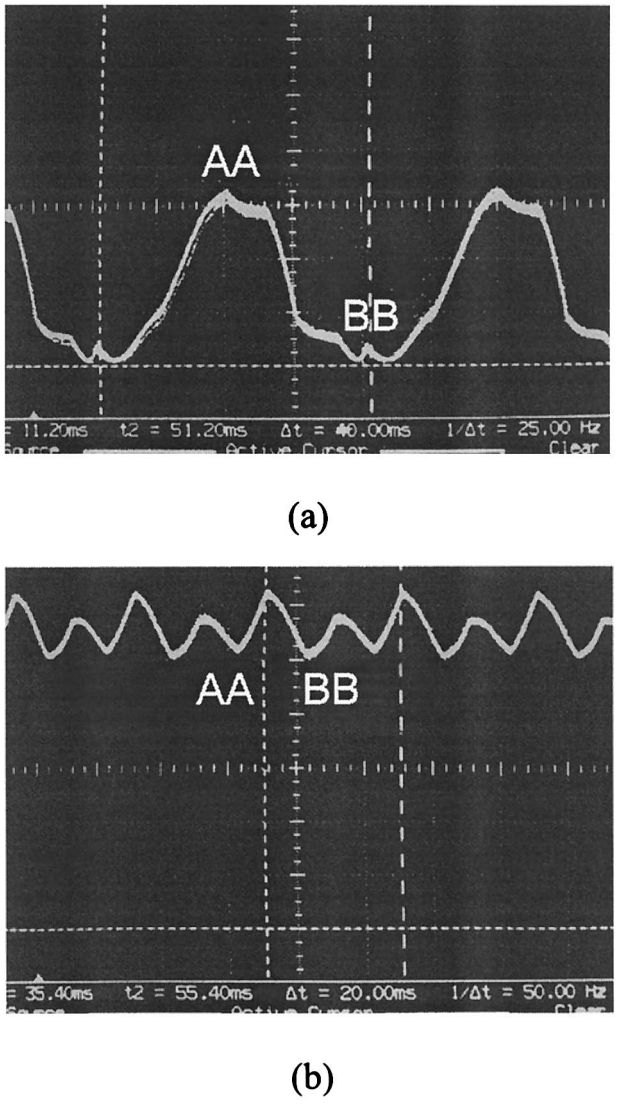

Fig. 7. Intensity variation trace: (a) One field is set to gray-scale value 255 and the other to gray-scale value zero; (b) both fields set to gray-scale value 255.

4. Electronics Development

A. Two-Dimensional Fast Fourier Transform Board

Computation of the phase of the FT of the input scene is required at video frame rates (i.e., 25 frames/s or 40 ms/image). This is a computationally demanding task, given the 512×512 image sizes. To complete this task, specialized FFT digital hardware was designed and built.

The FFT subsystem was centered around the Sharp/Butterfly Model LH9124 digital signal processor. This device incorporates radix 2, 4, and 16 butterfly structures, which are the building blocks for the FFT computations. It also has a specialized multiple-port bus architecture to handle complex arithmetic and rapid transfer of coefficient and image data. Fast fixed-point operations are supported, since the data buses are 48 bits wide, allowing for a wide dynamic range. This device is capable of computing a 512×512 FFT in 39.9 ms. Since the input data are real in nature, improved speed performance can be achieved through the exploitation of the symmetry of the resulting output data. Taking advantage of these features permits the FFT to be

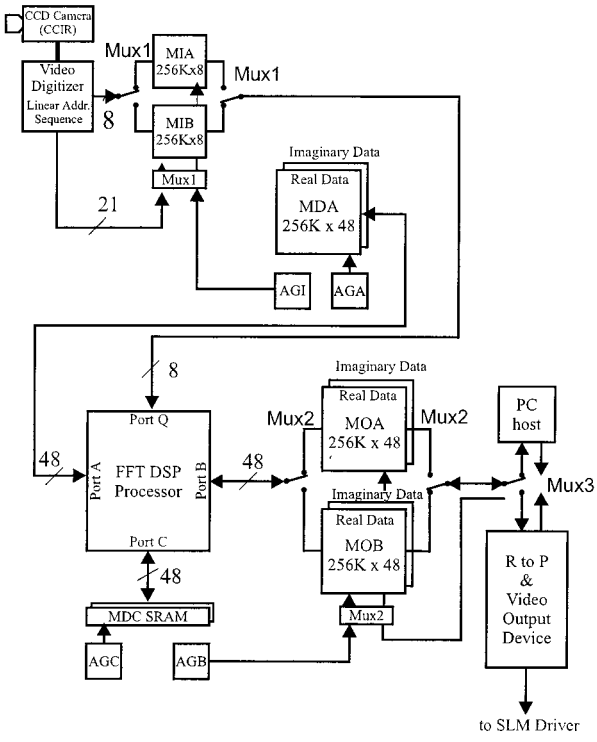

Fig. 8. Architecture of the FFT hardware, showing data flow and major components and data buffering to enable sustained real-time operation.

computed in 31 ms. However, the data input and output transfer schemes are consequently made more complicated.

In addition to the LH9124 digital signal processor, the design incorporates four high-speed microprocessors to provide the specialized memory address patterns, multiple high-speed memory buffers with 15-ns access time, and a Pythagoras chip to convert the real and the imaginary output data values to phase values. The architecture of the system is shown in Fig. 8 and was dominated by the necessity to multiplex large memories for manipulating the temporary data arrays. The PC ISA bus is used to provide a convenient means of initializing the system board. The high-speed data transfers (image input and image output) are performed by means of dedicated input–output ports to supplementary imaging boards. The completed hardware is shown in Fig. 9. Correct computation of both 256×256 and 512×512 FFT's was validated by comparison with numerically simulated FFT's.

Two of the programmable-gate-array- (PGA-) based imaging boards are incorporated into the FFT system. One is used to capture an image from the CCIR CCD camera viewing the input scene. The image is passed on to the FFT system in bit-reversed order. The second imaging board receives the output image from the FFT system and is responsible for the correct display of this data on the SLM device.

B. High-Frame-Rate Correlation Plane Processing

Each time a correlation between the input and a database image is performed, a correlation-plane output image is produced. The location of the correlation peak identifies the position of the object in the input scene. The correlation-plane processing task is to discriminate between good and poor correlations. This task must be completed at a rate of 2900 decisions/s, corresponding to the maximum frame rate of the 64×64 pixel array DALSA Model CA-D1-0064 digital camera used in analyzing the correlation plane.

The hardware architecture of the imaging board exploits the ability of the PGA's to tackle the computationally demanding tasks that must be performed on every pixel in the image (e.g., summation, counting, comparisons, and logic operations). Functions such as divisions, which are not required for every pixel, are executed by a host central processing unit (CPU).

The functional architecture is shown in Fig. 10. The main components are the PGA processors, mul-

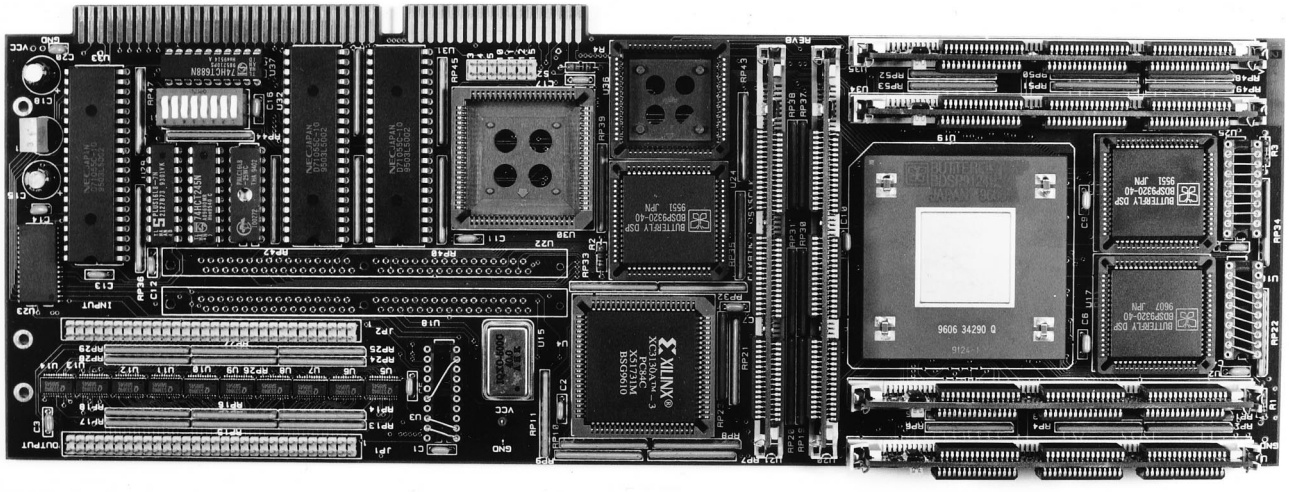

Fig. 9. Completed FFT subsystem hardware.

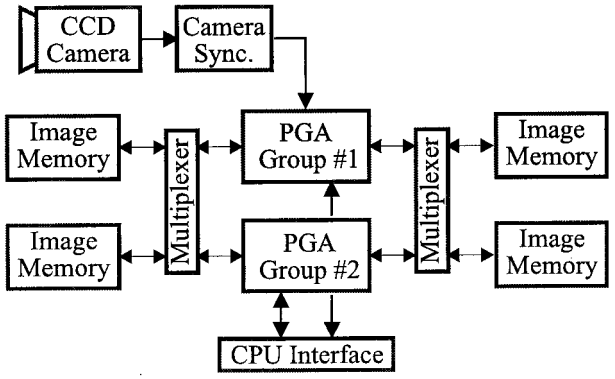

Fig. 10. Correlation-plane processing hardware architecture.

tiplexers, high-speed memory, and supporting interfaces. The division of the hardware into two computational groups (phase 1 and phase 2) greatly enhances the ability to implement more-sophisticated real-time algorithms. During the period in which phase-1 processing is implemented on the incoming raw data for the current frame period, the phase-2 data processing stage is implemented with the image captured during the previous frame period together with the results from the phase-1 processing of that image.

Careful planning of the internal routing permits fast logic and registers to be implemented with the combinational logic blocks available in the XiLinx Model 3130 PGA device.

The first phase of processing determines a threshold level for the input image. It is necessary that this threshold be adaptable to compensate for variations in the light intensity of the correlation image, which changes with different database image search strategies, essentially filtering out the noise floor. The output from this process is a binary image where all pixels greater than the threshold are mapped to 1 (labeled ON pixels) and all others to 0 (labeled OFF pixels). It is the assessment of the ON pixels in the phase-2 processing that quantifies the correlation quality and location.

A more-complicated algorithm is implemented in phase 2 where multiple correlation peak parameters are derived as shown in Tables 1 and 2.[14] The result is a peak density parameter, nDensity, which is used to quantify the quality of the correlation peak. The peak density is a function of the number of UP pixels and also the extent of the area these pixels occupy; i.e., if the UP pixels are in close proximity to one another, the score is higher than if the UP pixels are dispersed.

The performance of the system was evaluated with the digital camera operating at 2900 frames/s. The pixel data clock speed is 16 MHz, which determines the clock speed for phase-1 processing. The longest PGA task requires 103 μs, which is well within the 345-μs camera frame period. The few computations performed by the host CPU add an additional 4 μs to the algorithm execution time. Initial validation of the high-speed operation of the algorithm was demonstrated through the accurate tracking of small markers simulating the correlation peaks placed on a disk driven at high rotation rates to simulate movement of the correlation peak. Under test, the measured values of the (x, y) location of the peak produced the anticipated result of simple sine and cosine variation, respectively, thus validating the PGA algorithms at full frame rate operation.

C. Correlator Control and Coordination System

The control of the correlator operation relies on the precise coordination of the subsystems. The functions can be arranged into three functional groups—all operating at video frame rates. Contained within the second group are the high-speed operations associated with the search of the optical database:

1. The input scene viewed by a CCD camera is digitized, the phase of the Fourier transform computed, and the result displayed on a phase-modulating SLM.
2. For each input image a series of processing steps are completed to search a database of reference templates at high speed.

Table 1. Image Parameters Computed in Parallel by Imaging Board PGA's

Parameter	Description
xMin, xMax yMin, yMax	Minimum and maximum coordinates of target bounding box
xSum, ySum	Summation of x–y coordinate of all target pixels
nSize	Number of pixels set to 1 in target

Table 2. Image Parameters Computed by the Host CPU

Parameter	Description	Formula
xGravity	Mean x–y position of the target	$x\text{Gravity} = x\text{Sum}/n\text{Size}$
yGravity		$y\text{Gravity} = y\text{Sum}/n\text{Size}$
nDensity	Concentration index of all pixels set to 1 in target	$n\text{Density} = \dfrac{n\text{Size}}{(x\text{Max} - x\text{Min})(y\text{Max} - y\text{Min})}$

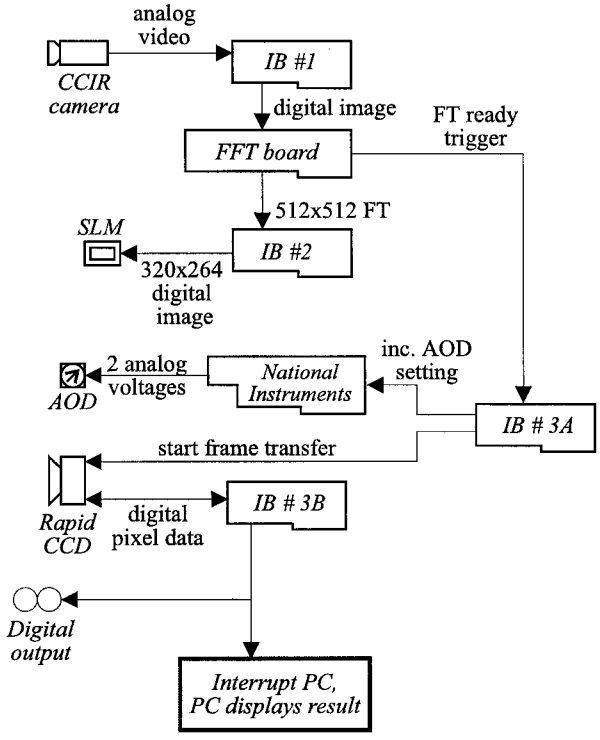

Fig. 11. Overview of digital subsystems and their coordination (IB, imaging board).

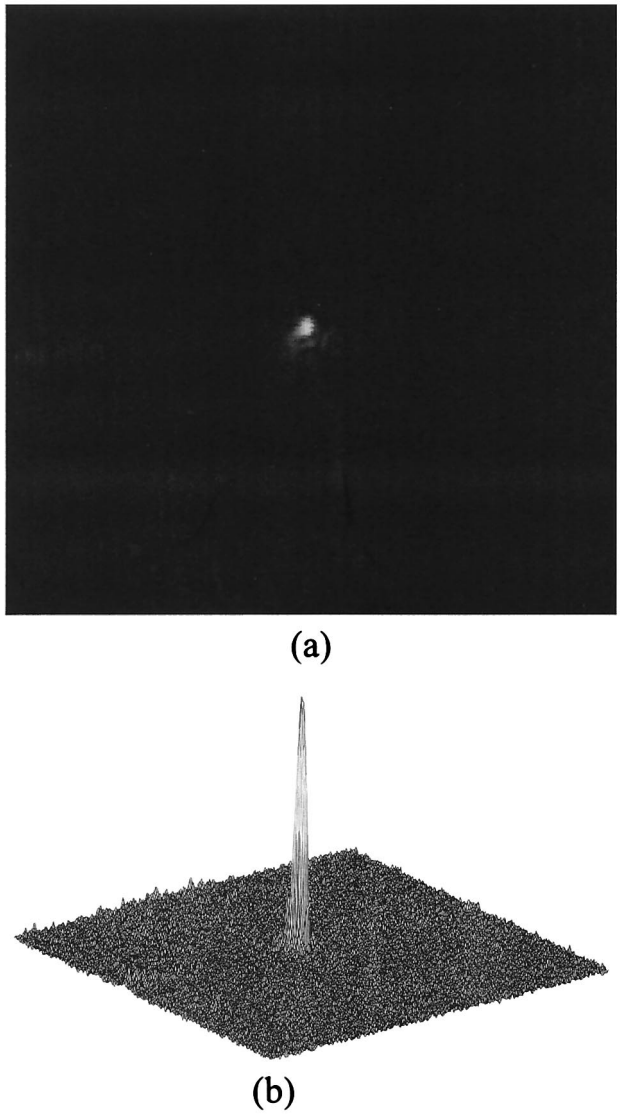

Fig. 12. Autocorrelation of the test component at 0° out-of-plane rotation and 20° in-plane rotation: (a) as captured correlation-plane image; (b) enlarged three-dimensional plot of correlation peak.

- The reference templates are reconstructed by setting of the appropriate control voltages to the AOD. This addresses the angle-multiplexed volume holographic memory by changing of the incident angle of the laser beam.
- The reconstructed reference template is input into the optical correlator; the correlation of the input scene with the reference template is generated and captured by the rapid CCD camera.
- Fast digital processing then determines the quality and the location of peaks in the captured correlation plane images.

3. The best correlation result is used to determine the identity and location of the object.

The electronic hardware involved in these processes is shown in Fig. 11. The synchronization of the subsystems is arranged in a pass-the-baton format. The first subsystem is triggered by the 25-Hz signal from the input CCD camera. Thereafter each subsystem initiates the next subsystem when the current task has completed.

The FFT subsystem is responsible for capture of the input scene, the computation of the phase of the FT, and its display on the SLM. After the image has been displayed, the search control subsystem is triggered. This system generates a series of signals to control an analog-to-digital converter that sets the AOD angle and also initiates the correlation-plane processing subsystem. An output response is generated for every input scene. The format of the output response is dependent on the application but can include information such as the identity of the best-matching database reference template, object identification, or location in the (x, y) plane.

5. Experimental Results

Initial testing of the correlator system was undertaken with a relatively small subset of images with 0° out-of-plane rotation. An autocorrelation result with the correlator is shown in Fig. 12. Note that these images are sections of the correlation plane captured with a standard CCD camera to provide high-resolution, detailed examination of the correlation behavior rather than with the low-resolution 64×64 pixel high-speed device that is used during correlator operation. It can be seen from this figure that the correlation peak is clearly visible with a good

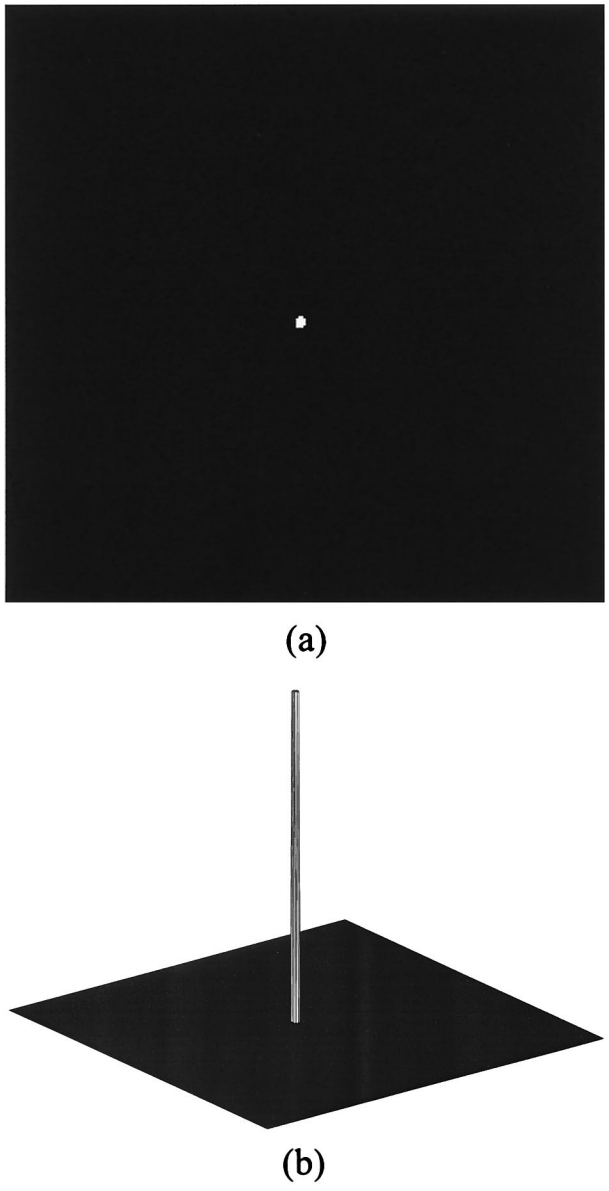

Fig. 13. Autocorrelation result of Fig. 12 after thresholding. (a) Correlation plane. (b) Isometric view of correlation peak.

signal-to-noise ratio. Passing the correlation-plane image through the correlation-plane processing system produced the thresholded image as shown in Fig. 13, where the correlation-peak height has been normalized. The nDensity parameter characterizing this result is 0.85, which compares well with the ideal case of nDensity = 1.

Cross correlation between the image used above and images of the component rotated by a further 5° failed to produce a clearly defined correlation peak above the noise floor. Simulation results indicate that, although the correlation-peak height may be expected to be reduced, the peak should still be clearly distinguished. Simulation assumes, of course, an ideal phase response from the SLM. During operation, however, it was found that, along with the nonlinear dynamic response curve shown in Fig. 6, the response of the SLM is spatially nonuniform. This may have imposed a serious constraint on the operation of the correlator, and real-time digital correction of this effect is the subject of future investigation.

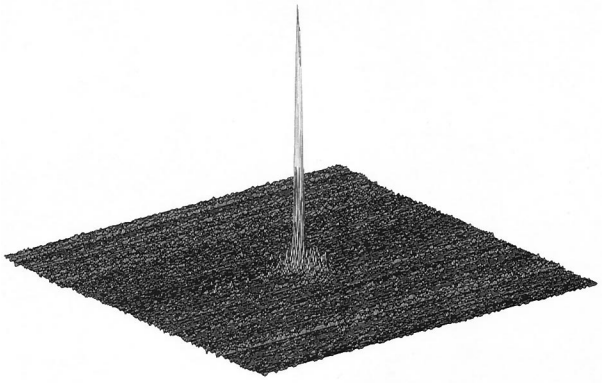

Fig. 14. Autocorrelation of suboptimal OT-SDF.

Recordings were then made of the suboptimal OT-SDF filters. Figure 14 shows the autocorrelation of

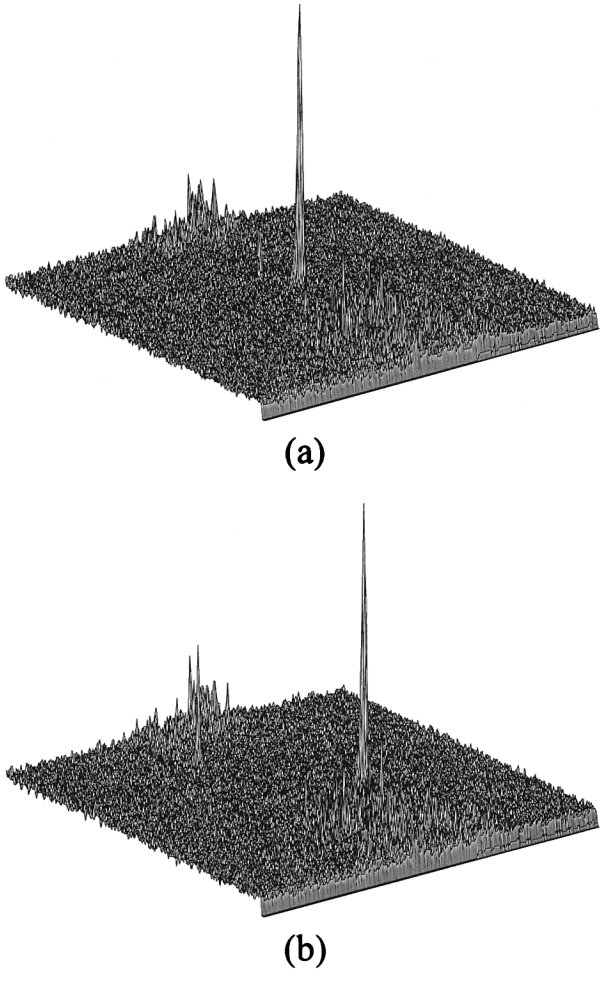

Fig. 15. Correlation-plane response to translation of the component in the input image: (a) is translated by 15 pixels horizontally and vertically with respect to the result shown in (b).

this filter. Again, as we would expect from a phase-only correlation, the correlation peak is sharp and provides good localization. The signal-to-noise ratio is also at an acceptable level with the peak quite clearly defined. For this result we obtained nDensity = 0.78. As may be expected from the previous cross-correlation response, cross correlation with these filters gave poor correlation-plane images, producing no clearly distinguished peak. It is anticipated that this will be greatly improved once the imaging board architecture incorporates the necessary real-time correction for response inhomogeneity.

Correlator performance as a function of component translation was then studied. As can be seen in Fig. 15, which shows enlarged sections of the correlation-plane images, the anticipated corresponding translation of the correlation peak is exhibited. The peak remains clearly distinguishable above the noise background. Note, however, that, since the images in the optical memory were not fixed, the resulting partial erasure has produced additional scattering in the optical train giving, rise to an increased background noise level.

6. Conclusions

A high-speed hybrid optical–digital correlator system capable of operation at approximately 3000 correlations/s has been demonstrated. Central to the operation of this correlator is the high-speed addressing of high-fidelity images from the phase-conjugating optical memory coupled with the custom-designed digital FFT processing board and rapid correlation-plane processing that uses a parallel processing architecture.

The authors acknowledge the support of this study by the European Commission through the Brite-EuRam program, contract BRE2-CT93.

Appendix A: Nonuniformity of Spatial Light Modulators

Tables 3, 4, and 5 show the nonuniformity of red, green, and blue channel SLM's, respectively.

Table 3. Nonuniformity of Red Channel SLM (Phase in Radians)

x/mm \ y/mm	0.0	2.5	5.0	7.5	10.0	12.5	15.0	17.5
0.0	−0.22	−0.39	−0.28	−0.28	−0.17	0.00	0.00	0.22
2.5	−0.22	−0.39	−0.28	−0.17	−0.06	0.11	0.17	0.22
5.0	−0.22	−0.22	−0.17	−0.11	−0.06	0.34	0.22	0.39
7.5	−0.11	−0.17	−0.11	−0.11	0.06	0.34	0.28	0.39
10.0	−0.11	−0.11	−0.17	−0.06	0.11	0.34	0.50	0.39
12.5	−0.11	−0.22	−0.22	−0.17	0.11	0.34	0.56	0.39
15.0	−0.11	−0.17	−0.22	−0.17	0.06	0.28	0.61	0.39
17.5	−0.11	−0.06	−0.17	−0.17	0.00	0.06	0.50	0.17
20.0	−0.17	−0.11	−0.11	−0.22	−0.11	−0.06	0.22	0.11
22.5	−0.11	−0.17	−0.28	−0.22	−0.17	−0.11	0.11	0.11

Table 4. Nonuniformity of Green Channel SLM (Phase in Radians)

x/mm \ y/mm	0.0	2.5	5.0	7.5	10.0	12.5	15.0	17.5
0.0	−0.30	0.15	−0.15	0.00	0.00	0.00	−0.15	−0.15
2.5	0.45	0.00	0.00	0.00	0.00	0.00	−0.15	0.00
5.0	−0.30	0.00	0.00	0.00	−0.15	0.00	−0.15	−0.15
7.5	0.15	0.00	0.00	0.00	0.00	0.00	−0.15	−0.15
10.0	0.15	0.00	0.00	0.00	0.00	0.00	−0.30	−0.15
12.5	0.00	0.00	0.15	0.00	0.00	0.00	−0.30	−0.15
15.0	0.00	0.00	0.15	0.00	0.00	0.00	−0.15	−0.15
17.5	0.00	−0.15	0.15	0.00	0.00	0.00	−0.15	−0.30
20.0	−0.15	0.15	0.15	0.15	0.15	0.15	−0.15	−0.30
22.5	−0.15	−0.15	0.15	0.15	0.15	0.15	−0.15	−0.30

Table 5. Nonuniformity of Blue Channel SLM (Phase in Radians)

x/mm \ y/mm	0.0	2.5	5.0	7.5	10.0	12.5	15.0	17.5
0.0	1.32	0.88	0.66	−0.99	−0.99	0.44	0.55	1.76
2.5	1.54	0.66	0.22	−0.77	−1.21	0.44	0.66	1.76
5.0	1.43	0.44	0.00	−0.55	−1.10	0.99	0.88	1.98
7.5	1.43	0.55	−0.22	−0.11	−1.10	0.99	1.32	1.98
10.0	1.43	0.77	−0.33	0.11	−0.88	0.66	1.65	1.76
12.5	1.43	1.21	−0.55	0.22	−0.55	0.66	1.87	1.76
15.0	1.32	1.54	−0.44	0.44	0.55	0.55	1.87	1.76
17.5	1.54	1.76	0.11	0.55	0.22	0.44	1.76	1.87
20.0	2.09	1.98	0.55	0.66	0.22	0.00	1.43	2.09
22.5	2.20	1.98	0.77	0.66	−0.22	−0.11	1.10	2.64

References and Note

1. D. C. Burns, I. Underwood, A. O'Hara, and D. G. Vass, "Electronically addressed ferroelectric liquid crystal spatial light modulators," Inst. Phys. Conf. Serv. **139,** 543–546 (1995).
2. L. J. Hornbeck, "Deformable-mirror spatial light modulators," in *Spatial Light Modulators and Applications III*, U. Efron, ed., Proc. SPIE **1150,** 86–102 (1989).
3. T. Yamashita, T. Shimada, Y. Akebi, T. Matsumoto, K. Tsubota, K. Fujioka, and Y. Takafuji, "Very small HDTV poly-Si TFT-LCD with fully integrated drivers," **56,** 43–46 (1993).
4. B. V. K. Vijaya Kumar, "Tutorial survey of composite filter designs for optical correlators," Appl. Opt. **31,** 4773–4801 (1992).
5. B. V. K. Vijaya Kumar, "Minimum variance synthetic discriminant functions," J. Opt. Soc. Am A **3,** 1579–1584 (1986).
6. A. Mahalanobis, B. V. K. Vijaya Kumar, and D. Casasent, "Minimum average correlation energy filters," Appl. Opt. **26,** 3633–3640 (1987).
7. R. R. Kallman, "Construction of low noise optical correlation filters," Appl. Opt. **25,** 1032–1033 (1986).
8. P. Réfrégier, "Optimal trade-off filters for noise robustness, sharpness, and Horner efficiency," Opt. Lett. **16,** 829–831 (1991).
9. S. Tonda, "Design of sub-optimal filters for optical implementation," BRITE-EURAM project RY1, Tech. Rep. T413–2, doc. ref. RY1/TR/TSN/ST961212 (Thomson-CSF, Paris, 1996).
10. V. Laude and Ph. Réfrégier, "Multicriteria characterization of coding domains with optimal Fourier spatial light modulator filters," Appl. Opt. **33,** 4465–4471 (1994).
11. R. C. D. Young, C. R. Chatwin, and B. F. Scott, "High-speed hybrid optical digital correlator system," Opt. Eng. **32,** 2608–2615 (1993).

12. J. H. Sharp, D. M. Budgett, P. C. Tang, and C. R. Chatwin, "An automated recording system for page oriented volume holographic memories," Rev. Sci. Instrum. **66,** 1–4 (1995).
13. J. H. Sharp, D. M. Budgett, C. R. Chatwin, and B. F. Scott, "High-speed, acousto-optically addressed optical memory," Appl. Opt. **35,** 2399–2402 (1996).
14. D. M. Budgett, P. E. Tang, J. H. Sharp, C. R. Chatwin, R. C. D. Young, R. K. Wang, and B. F. Scott, "Parallel pixel processing using programmable gate arrays," Electron. Lett. **32,** 1557–1559 (1996).
15. M. Duelli, A. R. Pourzand, N. Collings, and R. Dandliker, "Pure phase correlator with photorefractive filter memory," Opt. Lett. **22,** 87–89 (1997).
16. S. Tonda, "Design of sub-optimal filters for optical implementation," BRITE-EURAM project RY1, Tech. Rep. T413–2, doc. ref. RY1/TR/TSN/ST961212 (Thomson-CSF, Paris, 1996).
17. Crystals sourced from Fujian Castech, Deltronic Inc., and the Optical Material Research Centre, Strathclyde University, UK.
18. F. H. Mok, M. C. Tackitt, and H. M. Stoll, "Storage of 500 high-resolution holograms in a $LiNbO_3$ crystal," Opt. Lett. **16,** 605–607 (1991).
19. Y. Taketomi, J. E. Ford, H. Sasaki, J. Ma, Y. Fainman, and S. H. Lee, "Incremental recording for photorefractive hologram multiplexing," Opt. Lett. **16,** 1774–1776 (1991).
20. H. Sasaki, Y. Fainman, and S. H. Lee, "Gray-scale fidelity in volume-multiplexed photorefractive memory," Opt. Lett. **18,** 1358–1360 (1993).
21. H. Kogelnik, "Coupled wave theory for thick hologram gratings," Bell Syst. Tech. J. **48,** 2909–2947 (1969).
22. A. R. Pourzand and N. Collings, "Detailed experiments on phase modulating SLM characteristics," 1995, BRITE-EURAM project RY1, Suppl. Tech. Rep. T213–1, doc. ref. RY1/TR/NCH/NC&ARP950523 (University of Neuchâtel, Neuchâtel, Switzerland, 1995).
23. J. C. Kirsch, D. A. Gregory, M. W. Thie, and B. K. Jones, "Modulation characteristics of the Epson liquid crystal television," Opt. Eng. **31,** 963–970 (1992).
24. D. A. Gregory, T. D. Hudson, and J. C. Kirsch, "Measurement of spatial light modulator parameters," in *Hybrid Image and Signal Processing II*, D. P. Casasent and A. G. Tescher, eds., Proc. SPIE **1297,** 176–185 (1990).
25. V. Laude, S. Mazé, P. Chavel, and Ph. Réfrégier, "Amplitude and phase coding measurements of a liquid crystal television," Opt. Commun. **103,** 33–38 (1993).
26. K. Ohkubo and J. Ohtsubo, "Evaluation of LCTV as a spatial light modulator," Opt. Commun. **102,** 116–124 (1993).
27. J. L. McClain, P. S. Erbach, D. A. Gregory, and F. T. S. Yu, "Spatial light modulator phase depth determination from optical diffraction information," Opt. Eng. **31,** 951–954 (1996).
28. "FLUKE: 100 Hz enhanced definition TV testing," application note (Fluke Corporation, Everett, Wash., 1994).